**Journal of Science and Technology – Engineering and Technology for Sustainable Development**
*Volume 35, Issue 4, October 2025, 009-016*

# First-Principles Study on the Electronic Structure and Optical Properties of $\alpha$-$(Al_xGa_{1-x})_2O_3$ Alloys

***Nguyen Le Manh An, Do Dang Minh, Nguyen Duc Hoang, Pham Mai Khanh, Nguyen Hong Hai, Hoang Thi Ngoc Quyen, Dao Hong Bach, Ha Minh Tan****
*School of Materials Science and Engineering, Hanoi University of Science and Technology, Ha Noi, Vietnam*
**Corresponding author email: tan.haminh@hust.edu.vn*

**Abstract**

*The study focuses on exploring the exceptional electronic and optical properties of the α-$(Al_xGa_{1-x})_2O_3$ alloys (AlGaO) using advanced density functional theory (DFT) with hybrid functional methods. By varying the Al content (x) from 0 to 1, the bandgap expands from 5.288 eV to 8.819 eV while maintaining its direct nature. The incorporation of Al significantly enhances the material's ability to absorb high-energy ultraviolet-light, particularly in the deep ultraviolet region (wavelength < 200 nm), due to the strong covalent nature of Al-O bonds and the widened conduction band. The absorption spectra exhibit a distinct shift toward higher energies as the Al ratio increases, accompanied by pronounced optical anisotropy along the x and z crystallographic directions. These characteristics highlight the alloy's flexible tunability, making it an ideal candidate for advanced applications such as ultraviolet band-C (UVC) sensors, germicidal light sources, and anti-reflective coatings. This study not only provides a solid theoretical foundation for optimizing α-$(Al_xGa_{1-x})_2O_3$ as a versatile wide-bandgap semiconductor but also paves the way for future experimental studies to fully unlock its potential in next-generation electronic and optoelectronic devices.*

Keywords: AlGaO alloys, density functional theory, ultra-wide bandgap semiconductors, electronic structure, UVC absorption.

## 1. Introduction

Wide bandgap semiconductors are essential for the advancement of modern electronic and optoelectronic devices, enabling high-power electronics, ultraviolet (UV) detectors, and transparent conducting materials [1-2]. Among these, $Ga_2O_3$ and $Al_2O_3$ stand out for their unique electronic and optical properties. Specifically, the α-phase of $Ga_2O_3$, with its corundum-like structure [2-4], offers an ultra-wide bandgap (~5.3 eV), making it ideal for high-voltage and UV emission applications [5]. Similarly, $Al_2O_3$, with an even wider bandgap of approximately 8.8 eV, enhances its role as a dielectric material and UV-transparent substrate.

Combining $\alpha$-$Ga_2O_3$ and $\alpha$-$Al_2O_3$ into $\alpha$-$(Al_xGa_{1-x})_2O_3$ provides a tunable alloy system with adjustable bandgap and dielectric properties [5]. This makes it suitable for applications in extreme environments, such as high temperatures, and highlights its potential as a candidate for advanced electronic and optoelectronic devices [6]. However, research on the $\alpha$-phase of this alloy is still limited, particularly regarding its lattice structure, electronic structure, and optical behavior across varying Al compositions.

While significant research exists on the $\beta$-phase of $Ga_2O_3$ due to its thermodynamic stability and commercial relevance, studies on the $\alpha$-phase of $(Al_xGa_{1-x})_2O_3$ remain limited. Previous density functional theory (DFT) calculations on pure $\alpha$-$Ga_2O_3$ and $\alpha$-$Al_2O_3$ have provided insights into their electronic structures and optical behavior, as listed in Table 1. However, the combined effects of alloying these materials at varying Al ratios are not well understood. Furthermore, challenges in modeling such systems theoretically, along with discrepancies between experimental and theoretical predictions, necessitate advanced computational methods to accurately describe this alloy system [7].

This study aims to fill this gap by leveraging first-principles density functional theory to comprehensively analyze the electronic and optical properties of $\alpha$-$(Al_xGa_{1-x})_2O_3$ across a range of alloy compositions. Through these investigations, we seek to provide a theoretical foundation for optimizing this material for next-generation technologies in power electronics, deep-ultraviolet optoelectronics, and other advanced technologies where high performance and material reliability are paramount.

p-ISSN 3093-3242
e-ISSN 3093-3579
https://doi.org/10.51316/jst.185.etsd.2025.35.4.2
Received: Mar 3, 2025; Revised: Jul 7, 2025;
Accepted: Jul 31, 2025; Online: Sep 20, 2025.

Table 1. Calculated lattice parameters and band gaps of corundum structures $\alpha$-$Al_2O_3$ and $\alpha$-$Ga_2O_3$

| | | | $a = b$ (Å) | $c$ (Å) | $E_g$ (eV) |
|---|---|---|---|---|---|
| $\alpha$-$Al_2O_3$ | This work | | 4.775 | 13.015 | 8.8194 (d) |
| | Literature | Cal. | 4.77[8] | 13.013[8] | 8.56 (d)[8] |
| | | Exp. | 4.76[4] | 12.99[8] | 8.8[4] |
| $\alpha$-$Ga_2O_3$ | This work | | 4.999 | 13.441 | 5.29 (d)<br>5.05 (i) |
| | Literature | Cal. | 5.005[8] | 13.454[8] | 5.26(i)[8] |
| | | Exp. | 4.983[8] | 13.433[8] | 5.3 (d)[5,6]<br>5.02 (i)[6] |

*Note: The indirect and direct bandgaps are denoted as (i) and (d), respectively*

## 2. Modeling and Calculation Methods

Both $\alpha$-$Ga_2O_3$ and $\alpha$-$Al_2O_3$ polymorphs share the corundum crystal structure, belonging to the R$\bar{3}$c space group (No. 167 in the International Tables for Crystallography). Their conventional and primitive cells are illustrated in Fig. 1a and Fig. 1b, where Ga and Al atoms occupy octahedral sites coordinated by oxygen atoms. These structures highlight the similarities and differences in lattice parameters and atomic arrangement between $Ga_2O_3$ and $Al_2O_3$. The lattice constants differ by 3.54% along the $c$-axis and 4.81% along the $a$-axis for the hexagonal unit cell [8-10]. The lattice parameters of $\alpha$-$Ga_2O_3$ are: $a = b = 4.999$ Å, $c = 13.441$ Å, and those of $\alpha$-$Al_2O_3$ are: $a = b = 4.775$ Å, $c = 13.015$ Å, with angles $\alpha$ equal $\beta$ equal to 90° and $\gamma$ equal to 120°. Within the hexagonal unit cell, the oxygen ions form close-packed hcp layers, while the metal ions occupy two-thirds of the octahedral interstitial sites.

In this study, calculations for the $\alpha$-$(Al_xGa_{1-x})_2O_3$ alloys were performed using a conventional unit cell. This specific cell consists of 12 gallium (Ga) or aluminum (Al) atoms and 18 oxygen (O) atoms. Using a conventional cell, which is larger than a primitive cell, allows for the modeling of various alloy compositions by substituting Ga atoms with Al atoms. Each metal atom (Ga or Al) is surrounded by six O atoms, forming $MO_6$ (M = Ga, Al) octahedra. These octahedra share one face and three edges with adjacent octahedra. The conventional cells of $(Al_{0.25}Ga_{0.75})_2O_3$, $(Al_{0.5}Ga_{0.5})_2O_3$, and $(Al_{0.75}Ga_{0.25})_2O_3$ are illustrated in Fig. 1c, Fig. 1d, and Fig. 1e, respectively. The figures show the gradual substitution of Ga by Al in the alloy structure.

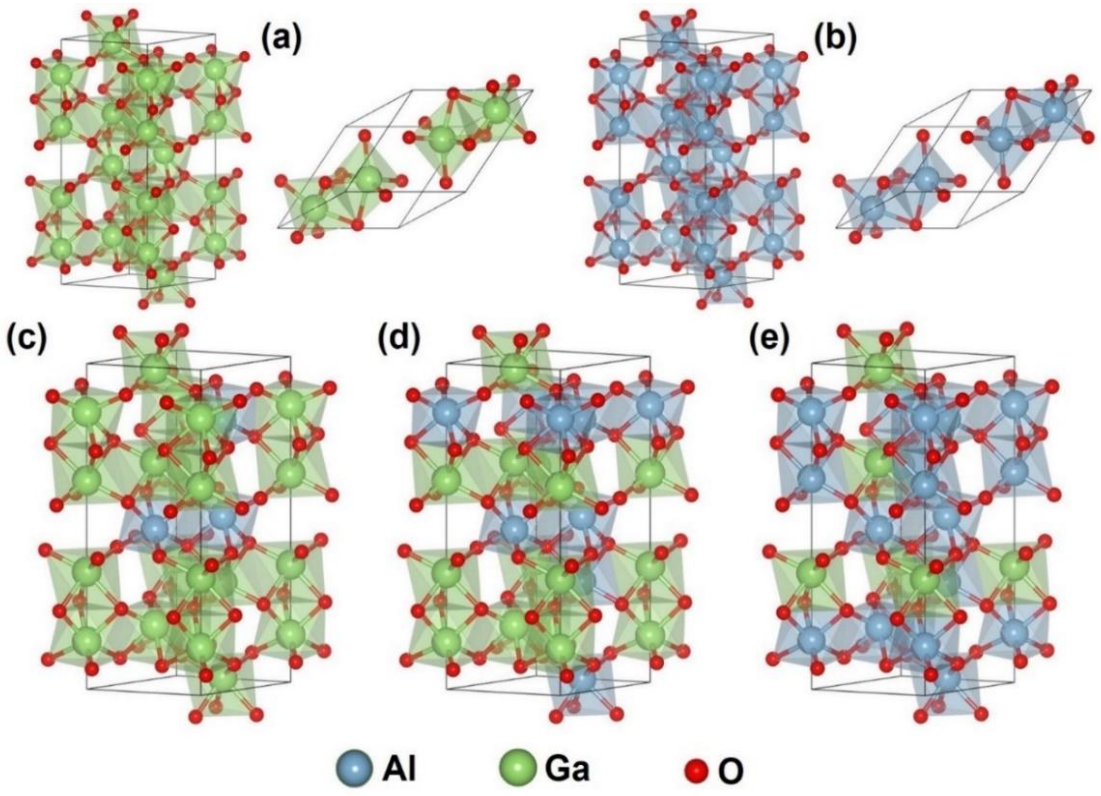


Fig. 1. The conventional (left) and the primitive (right) cells represent (a) $\alpha$-$Ga_2O_3$, (b) $\alpha$-$Al_2O_3$. Other examples of conventional cells of (c) $(Al_{0.25}Ga_{0.75})_2O_3$ (d) $(Al_{0.5}Ga_{0.5})_2O_3$ (e) $(Al_{0.75}Ga_{0.25})_2O_3$. (Ga atoms are shown in green, Al atoms in blue, and O atoms in red)

The electronic structure and optical properties of the $\alpha$-$(Al_xGa_{1-x})_2O_3$ alloy system were investigated using first-principles calculations based on DFT. DFT is a computational method in quantum physics and chemistry used to study the electronic structure of many-body systems. By focusing on the electronic density of the system, DFT simplifies the complex many-body quantum problem. With various approximations for the exchange-correlation potential, DFT offers an effective and practical tool for describing the electronic properties and structure of materials.

All calculations in this study were performed using the open-source QUANTUM ESPRESSO (QE) software package (under the GNU General Public License). QE is a fully integrated suite of codes for electronic structure calculations and material modeling, based on DFT with plane-wave basis sets and pseudopotentials to represent electron-ion interactions [11].

The $\alpha$-$(Al_xGa_{1-x})_2O_3$ structure was optimized using the PBEsol exchange-correlation functional and projector augmented wave (PAW) pseudopotentials. PBEsol, an improved version of the Perdew-Burke-Ernzerhof (PBE) functional, was specifically designed to enhance accuracy for calculations involving solids and surfaces. The kinetic energy cutoff for the wave function was set to 70 Ry, and the charge density cutoff was set to 560 Ry. Structural relaxation was carried out using the Broyden–Fletcher–Goldfarb–Shanno (BFGS)optimization algorithm, with convergence criteria for total energy of 1.0E-04 Ry, force of 1.0E-03 Ry/Bohr, and pressure of 0.5 kbar.

To achieve higher accuracy in the electronic structure calculations, the Heyd-Scuseria-Ernzerhof (HSE) hybrid functional was employed. In this approach, non-local Hartree-Fock exchange is mixed with the generalized gradient approximation (GGA) exchange for short-range interactions. The HSE functional was configured with a mixing parameter of 33% and a screening parameter of 0.106 $Bohr^{-1}$ for all calculations. The choice of these parameters was validated by the close agreement between the calculated bandgaps and experimental values for $\alpha$-$Ga_2O_3$ and $\alpha$-$Al_2O_3$ as presented in Table 1. The kinetic energy cutoff for the wave function, charge density, and self-consistent convergence threshold were set to 70 Ry, 560 Ry, and 1.0E-08 Ry, respectively. A Monkhorst-Pack *k*-point grid of 5×5×2 was used for Brillouin zone sampling in all calculations.

## 3. Results and Discussion

### *3.1. Structure Optimization*

The structural relaxation calculations for $\alpha$-$Ga_2O_3$ and $\alpha$-$Al_2O_3$ reveal significant lattice distortions as Al atoms replace Ga atoms within the corundum structure. Compared with experimental data and other calculations using the PBE method [8, 9], the results align well, confirming the reliability of the approach (Table 1). For $\alpha$-$Al_2O_3$, our calculated lattice parameters ($a$ = 4.775 Å, $c$ = 13.015 Å) differ from experimental values by only +0.3% and +0.2%, respectively. Similarly, for $\alpha$-$Ga_2O_3$, our calculated lattice parameter ($a$ = 4.999 Å, $c$ = 13.441 Å) show minimal differences of +0.3% and +0.06% compared to experimental measurements. Specifically, the smaller atomic radius of Al compared to Ga results in shorter Al-O bonds (approximately 1.85 Å) compared to Ga-O bonds (approximately 1.94 Å). This bond-length difference induces a contraction of the lattice, particularly along the *a*- and *c*-axes, as reflected in the reduced lattice parameters presented in Table 1. These structural changes highlight the impact of alloying on the lattice geometry and provide insight into the mechanisms driving property variations in the $\alpha$-$(Al_xGa_{1-x})_2O_3$ system.

In addition to bond shortening, the introduction of Al into the $\alpha$-$(Al_xGa_{1-x})_2O_3$ lattice induces local tilting and distortion of the $MO_6$ (M = Ga, Al) octahedra. These distortions are anisotropic, with stronger tilting effects along the *c*-axis due to the alignment of neighboring octahedra. At low Al concentrations ($x \leq 0.25$), Al atoms preferentially occupy octahedral sites adjacent to Ga atoms, minimizing lattice strain and stabilizing the structure. However, as the Al content increases ($x$ = 0.5), the mismatch in bond lengths between Ga-O and Al-O creates localized strain fields, resulting in more pronounced distortions.

At high Al concentrations ($x \geq 0.75$), the lattice becomes more uniform as most Ga atoms are replaced by Al. The Al-O bonds dominate, leading to a more compact and stable structure. This trend is consistent with Vegard's law, where the lattice parameters decrease linearly with increasing Al content.

The optimal incorporation of Al occurs when Al atoms substitute Ga atoms in a distributed manner, avoiding clustering. This configuration ensures a balance between lattice strain and structural stability, as shown in the relaxed configurations illustrated in Fig. 1c, Fig. 1d, and Fig. 1e. These findings emphasize the role of Al placement in tuning the structural and electronic properties of $\alpha$-$(Al_xGa_{1-x})_2O_3$.

As shown in Fig. 2a and Fig. 2b, the lattice parameters (a and c) of the alloy change linearly as the Al content increases, following Vegard's law. This relationship is expressed as:

$$d_{(Al_xGa_{1-x})_2O_3} = xd_{Al_2O_3} + (1-x)d_{Ga_2O_3} \qquad (1)$$

where *d* represents the lattice constant. The substitution of larger Ga atoms with smaller Al atoms leads to a contraction of the lattice, particularly along the *a*- and *c*-axes. Consequently, as Al content increases, the lattice constants decrease monotonically, and the unit cell volume shrinks (Fig. 2c), clearly demonstrating this contraction behavior.

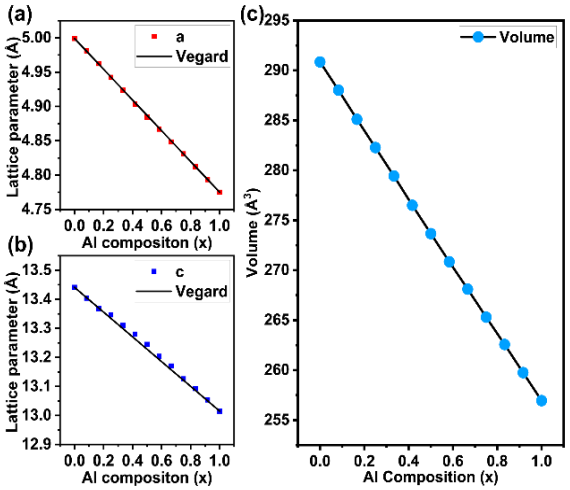


Fig. 2. (a) and (b) Lattice parameters $a$ and $c$ as functions of the Al composition; (c) Unit cell volume as a function of Al composition

### *3.2. Electronic Structure*

To further analyze the electronic structure, Fig. 3 and Fig. 4 provide insights into the band structure and partial density of states (PDOS) at various compositions.

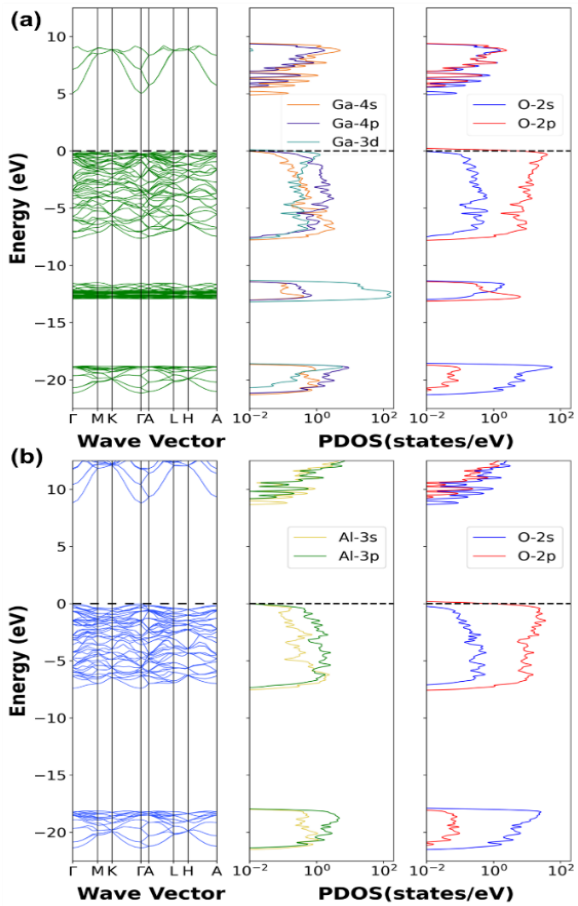


Fig. 3. Band structure and PDOS when (a) $x$ = 0, (b) $x$ = 1

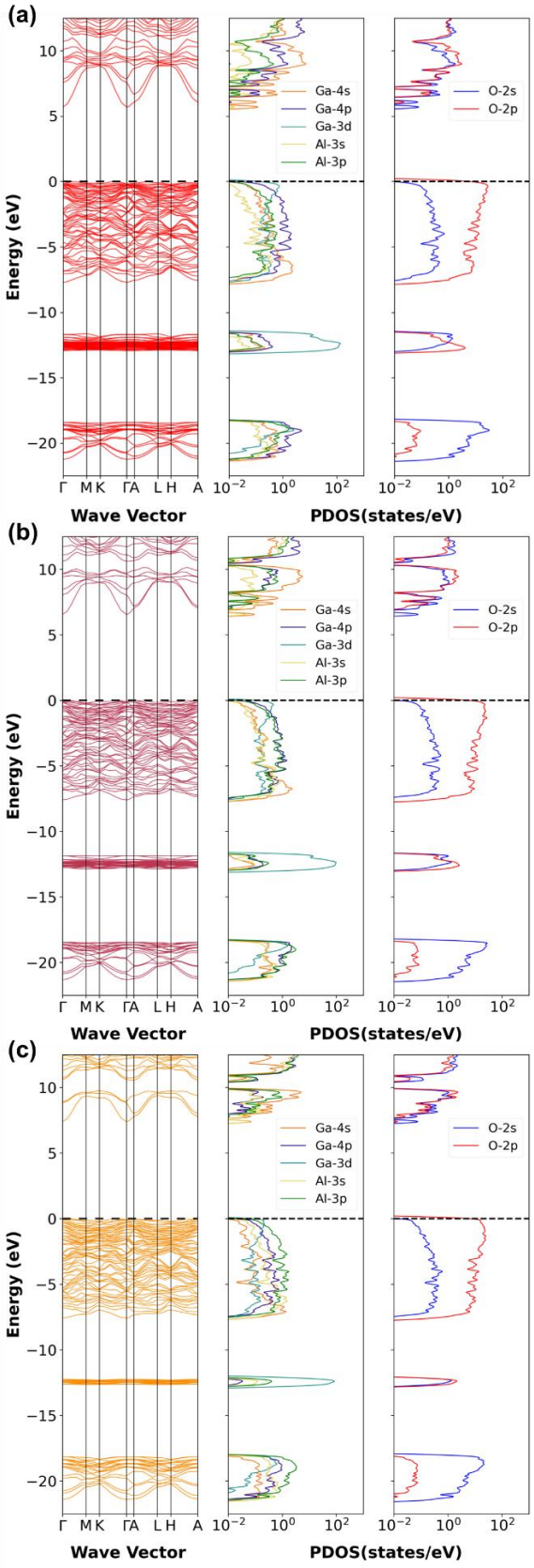


Fig. 4. Band structure and PDOS when (a) $x$ = 0.25, (b) $x$ = 0.5, (c) $x$ = 0.75

In Fig. 3, the band structures for $x$ equal to 0 and $x$ equal to 1 reveal distinct differences. For $x$ equal to 0, the valence band maximum (VBM) is dominated by contributions from Ga-3d and O-2p orbitals, while the conduction band minimum (CBM) comprises mainly Ga-4s states. These states contribute to the relatively smaller bandgap of $Ga_2O_3$. Conversely, at $x$ equal to 1, the CBM shifts significantly upward due to the dominant contribution of Al-3p orbitals. This transition leads to a much wider bandgap, emphasizing the role of Al in reshaping the alloy's electronic structure.

Fig. 4 expands this analysis to intermediate compositions ($x$ = 0.25, 0.5, 0.75), revealing a systematic progression in band structures and PDOS. As the Al content increases, the lattice is compressed due to the smaller atomic radius of Al compared to Ga. This compression strengthens the Al-O bonds, causing the CBM energy to rise. The PDOS analysis highlights a steady reduction in the contribution of Ga-3d orbitals to the VBM as $x$ increases, resulting in a narrower and less spread-out valence band. Simultaneously, the dominance of Al-3p orbitals at the CBM increases, directly correlating with the widening bandgap. The interplay between Ga-3d, Ga-4s, Al-3p, and O-2p orbitals, as seen in the PDOS, reflects a gradual transition from ionic Ga-O interactions to covalent Al-O interactions. This redistribution of electronic states alters the density of states near the VBM and CBM, directly impacting the optical properties of the alloy. The consistent direct bandgap across all compositions reinforces its potential for optoelectronic applications, such as UV photodetectors and lasers.

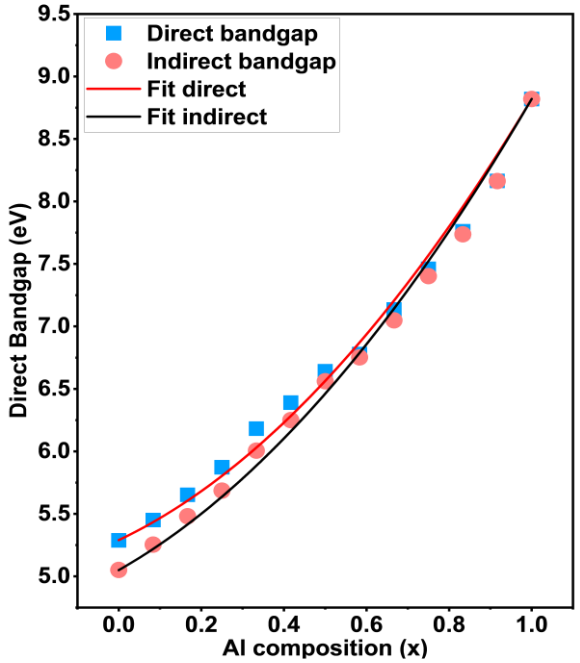


Fig. 5. Bandgap of the $\alpha$-$(Al_xGa_{1-x})_2O_3$ alloy at different Al compositions

DFT calculations for the bandgap of $\alpha$-$(Al_xGa_{1-x})_2O_3$ system, shown in Fig. 5, demonstrate a significant increase in the bandgap with rising Al content ($x$). At the endpoints of the composition range, our calculated bandgaps show agreement with experimental data (Table 1). Specifically, for pure $Ga_2O_3$ ($x$ = 0), the calculated direct bandgap is 5.288 eV, which is only 0.012 eV lower than the experimental value of 5.3 eV, and the indirect bandgap is 5.051 eV. For pure $Al_2O_3$ ($x$ = 1), the bandgap increases to 8.819 eV, just 0.019 eV higher than the experimental value of 8.8 eV, and becomes dominantly direct. Notably, in the composition range of $x$ from 0.75 to 0.83, the substantial increase in the direct bandgap to 7.4-7.7 eV enhances the material's effectiveness for UV-based technologies, including deep-UV lasers and optical communication systems.

The bandgap bowing parameter, $b$, is determined using the following equation:

$$E_g^{alloy} = (1-x)E_g^{Ga_2O_3} + xE_g^{Al_2O_3} - bx(1-x) \quad (2)$$

The value of $b$ was found to be 1.964 for the direct bandgap and 1.894 for the indirect bandgap, indicating a significant non-linear deviation from a linear interpolation of the bandgap energies. At high Al concentrations ($x$ > 0.75), the bandgap approaches values suitable for deep-UV (UVC) applications, exceeding 7.4 eV and reaching up to 8.819 eV for pure $Al_2O_3$. This makes the material an ideal candidate for high-energy UV devices, germicidal applications, and optical coatings with superior stability and efficiency in harsh environments.

### *3.3. Charge Density*

To analyze the redistribution of charge density in $\alpha$-$(Al_xGa_{1-x})_2O_3$ due to Al doping, the charge density difference $\Delta\rho(r)$ was calculated using the formula:

$$\Delta\rho(r) = \rho_{total}(r) - \sum_i \rho_{atoms,i}(r) \quad (3)$$

where $\rho_{total}(r)$represents the total charge density of the system, and $\rho_{atoms,i}(r)$ denotes the superposition of the charge densities of isolated atoms in their neutral states. This method isolates the redistribution of electronic charge caused by bonding interactions and doping effects within the lattice.

The charge density analysis, as shown in Fig. 6, uses the (110) crystallographic plane as the cross-sectional view. This plane provides a clear representation of the charge distribution around the O atoms and the dopant sites (Ga and Al). For pure $\alpha$-$Ga_2O_3$ (Fig. 6a), the charge density difference reveals a strong concentration of negative charge (red regions) around the O atoms, while the Ga atoms exhibit a more positive charge (blue regions), consistent with the ionic character of Ga-O bonds.

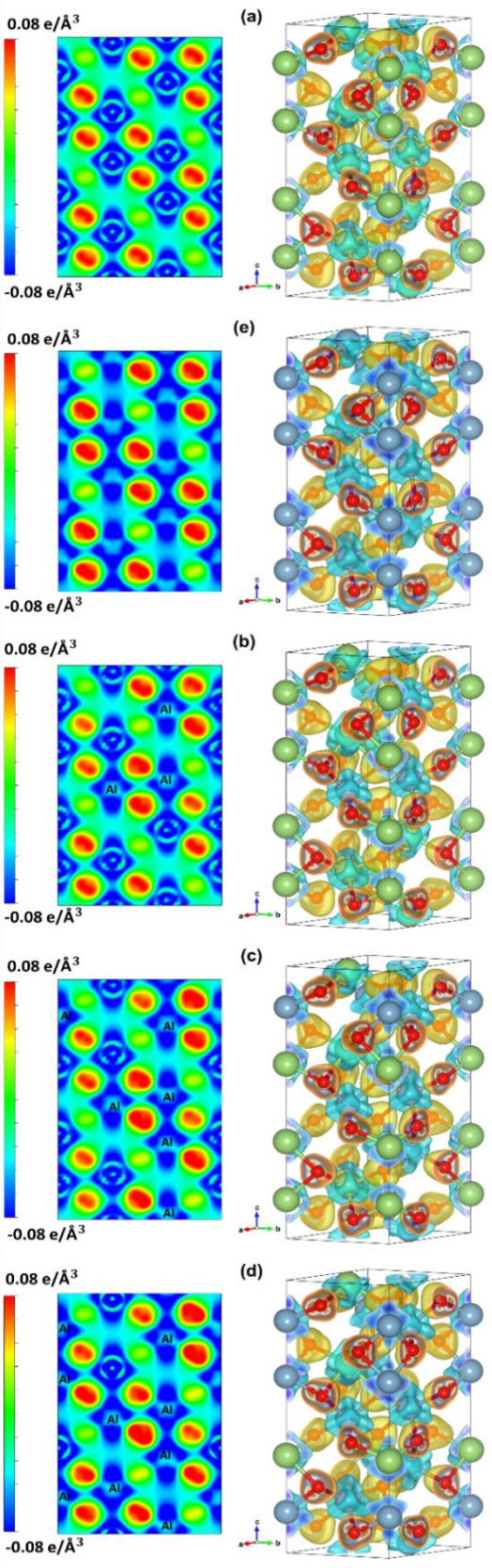


Fig. 6. Differential charge density distribution diagram for $\alpha$-$(Al_xGa_{1-x})_2O_3$ at different Al compositions: (a) $x$ = 0, (b) $x$ = 0.25, (c) $x$ = 0.5, (d) $x$ = 0.75, and (e) $x$ = 1

Upon substitution of Ga with Al (Fig. 6e), the red regions around O atoms and the blue regions around Al atoms appear lighter compared to Ga, indicating a weaker ionic interaction in Al-O bonds. This redistribution reduces the overall ionic character of the lattice and contributes to the widening of the bandgap.

At low Al concentrations ($x$ = 0.25, Fig. 6b), localized changes in charge density are observed. The substitution of Ga with Al results in a decrease in the charge density value around the Al atoms, while O atoms retain their dominant negative charge. As the Al concentration increases to $x$ equal to 0.5 (Fig. 6c), the charge distribution becomes more uniform, reflecting a more balanced contribution from Al-O and Ga-O bonds. For higher Al concentrations ($x$ = 0.75, Fig. 6d), the dominance of Al-O bonds leads to a noticeable decrease in charge density around the cation sites, indicating a significant alteration in the lattice's ionic interactions.

In summary, the charge density difference analysis using the (110) plane illustrates the progressive reduction in ionic interactions and the enhanced covalent nature of Al-O bonds as Al content increases. These changes contribute to the observed widening of the bandgap and significantly influence the electronic and optical properties of the $\alpha$-$(Al_xGa_{1-x})_2O_3$ alloy system.

### *3.4. Optical Properties*

The optical properties of the $\alpha$-$(Al_xGa_{1-x})_2O_3$ alloy, characterized by the dielectric function ($\varepsilon$), are strongly dependent on the Al concentration ($x$), as shown in Fig. 7. As $x$ increases, the primary absorption peaks in the imaginary part, Im($\varepsilon$), shift to higher energies. This shift directly reflects the widening of the material's bandgap. Concurrently, the intensity of these peaks decreases, indicating a reduction in the density of states (DOS) available for lower-energy photon interactions. The real part, Re($\varepsilon$), also shows a corresponding decrease, signifying reduced material polarizability consistent with the properties of $Al_2O_3$ compared to $Ga_2O_3$.

A notable characteristic revealed in Fig. 7 is the pronounced optical anisotropy of the alloy. The dielectric functions differ significantly along the $x$ and $z$ crystallographic directions, that is becomes more distinct with increasing Al content. For example, at $x$ equal to 1, the main peak in Re($\varepsilon$) is approximately 7.5 eV in the $z$-direction versus 7.3 eV in the $x$-direction, highlighting the anisotropic nature of the material's optical-electronic response.

The absorption spectrum analysis shown in Fig. 8 also clearly demonstrates the changes as the Al content in $\alpha$-$(Al_xGa_{1-x})_2O_3$ increases, for both $x$ and $z$ directions. This result is particularly important for understanding and exploiting the UVC absorption properties (wavelength from 100 to 280 nm). For $x$ equal to 0 ($Ga_2O_3$), the absorption spectrum is concentrated in the low energy range (approximately 5 eV, corresponding to

approximately 248 nm), mainly due to the Ga–O bonds. As the Al content increases, the absorption spectrum shifts to higher energies, reaching approximately 6 eV ($x$ = 0.25), 7 eV ($x$ = 0.5), and above 8 eV ($x \geq 0.75$). Particularly at $x$ equal to 1 ($Al_2O_3$), the absorption spectrum expands into the short UVC range (wavelength smaller than 150 nm, equivalently energy higher than 8.27 eV) due to the strong covalent Al–O bonds and the widening of the bandgap.

The peaks in the absorption spectrum reflect the main electronic transitions in the material. The peaks in the lower energy range (5–6 eV) represent basic transitions from the VBM to the CBM, and the intensity decreases as the Al content increases.

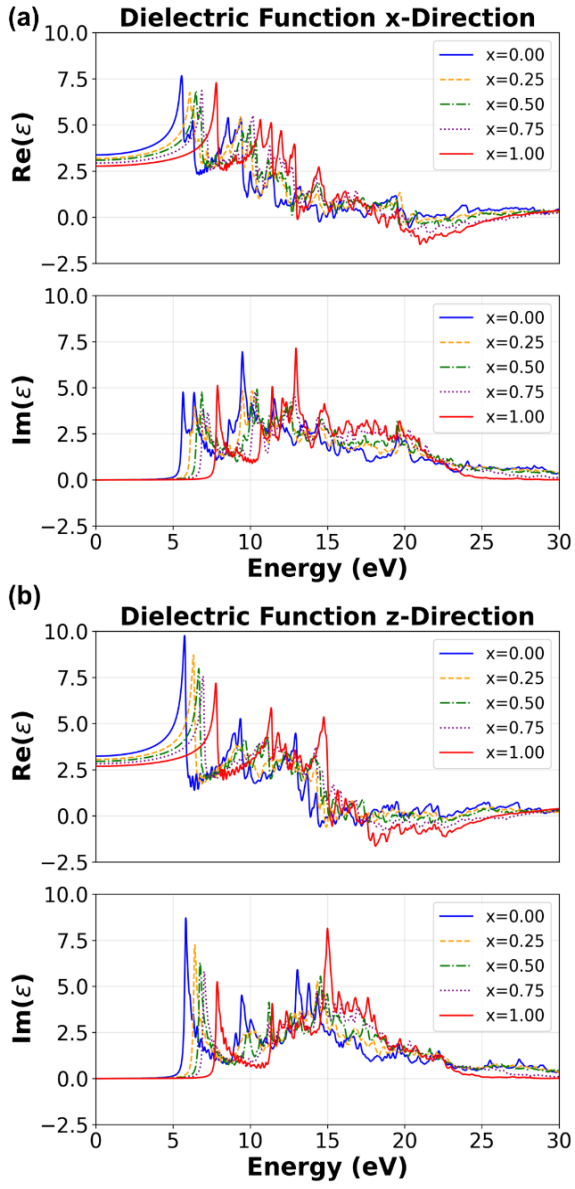


Fig. 7. Dielectric function, including the real part Re($\varepsilon$) and the imaginary part Im($\varepsilon$), for the $\alpha$-$(Al_xGa_{1-x})_2O_3$ alloy system at Al compositions $x$ = [0, 0.25, 0.5, 0.75, 1] along (a) the $x$-direction and (b) the $z$-direction.

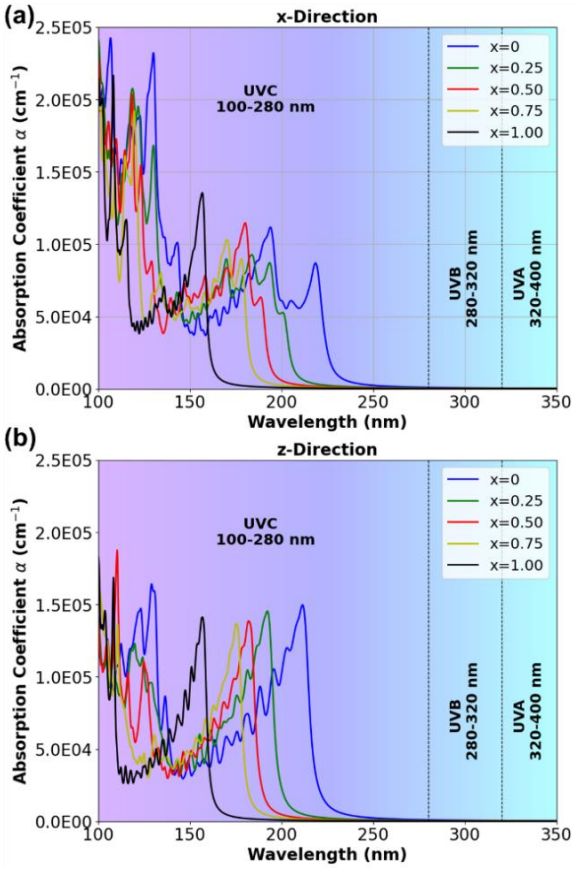


Fig. 8. Absorption spectra of $\alpha$-$(Al_xGa_{1-x})_2O_3$ along (a) the $x$-direction and (b) the $z$-direction.

Peaks in the medium energy range (6–7 eV) may be associated with direct electronic transitions or changes in the energy band structure due to Al doping, which becomes more pronounced as $x$ greater than or equal to 0.25. Peaks in the high-energy range (greater than 7 eV) reflect transitions from deeper states in the valence band, which are characteristic of Al-rich materials, with the ability to absorb high-energy light in the short UVC range (wavelength smaller than 150 nm).

The absorption spectrum in the $z$-direction reflects the anisotropy in the corundum crystal structure. These results confirm the ability to tune the absorption spectrum of $\alpha$-$(Al_xGa_{1-x})_2O_3$, making it an ideal candidate for optimizing materials for applications such as UVC light detectors, sterilization light sources, and anti-reflective optical coatings. The absorption peaks provide not only insights into the electronic structure but also pinpoint the specific wavelength regions suitable for each application.

## 4. Conclusion

This study provides a comprehensive understanding of the electronic and optical properties of the $\alpha$-$(Al_xGa_{1-x})_2O_3$ alloy, with a focus on the changes that occur as the Al content increases. The results show a continuous increase in the bandgap from

5.288 eV ($x$ = 0) to 8.819 eV ($x$ = 1), while maintaining the direct bandgap nature throughout the entire composition range. This makes the material suitable for applications that require high-energy light absorption, particularly in the short UVC range (wavelength smaller than 150 nm).

The presented absorption spectra and optical anisotropy demonstrate the material's flexible tunability with different Al concentrations. This not only optimizes the absorption properties but also opens up potential applications, such as UVC sensors, germicidal light sources, and anti-reflective optical coatings. The replacement of Ga-O bonds with Al-O not only strengthens the covalent bonding but also significantly alters the material's electronic structure and conduction band energy, thereby improving its optical performance.

These findings provide a solid theoretical foundation for optimizing wide-bandgap semiconductor materials and open up promising applications in high-performance optoelectronic devices.

**Acknowledgments**

This research was funded by the Vietnamese Ministry of Education and Training under grant number B2024-BKA-22.

**References**

[1] Roy, R., Hill, V. G., and Osborn, E. F., Polymorphism of $Ga_2O_3$ and the system $Ga_2O_3$–$H_2O$, Journal of the American Chemical Society, vol. 74, iss. 3, pp. 719–22, Feb. 1952. https://doi.org/10.1021/ja01123a039

[2] Kaneko, K., Aoki, Y., Tokuda, Y., and Higashiwaki, M., Progress in α-$Ga_2O_3$ for practical device applications, Japanese Journal of Applied Physics, vol. 62, Jun. 2023, Art. no. SF0803. https://doi.org/10.35848/1347-4065/acd125

[3] Yao, Y., Xia, X., Zhang, K. H. L., Gong, H., and Liu, Z., Growth and characterization of α-, β-, and ϵ-phases of $Ga_2O_3$ using MOCVD and HVPE techniques, Materials Research Letters, vol. 6, iss. 5, pp. 268–275, Mar. 2018. https://doi.org/10.1080/21663831.2018.1443978

[4] Ahmadi E., Oshima Y., Materials issues and devices of α- and β-$Ga_2O_3$, Journal of Applied Physics, vol. 126, iss. 16, Oct. 2019, Art. no. 160901. https://doi.org/10.1063/1.5123213

[5] Shinohara D & Fujita S., Heteroepitaxy of corundum-structured α-Ga2O3 thin films on α- $Al_2O_3$ substrates by ultrasonic mist chemical vapor deposition, Japanese Journal of Applied Physics, vol. 47, Sep. 2008, Art. no. 7311. https://doi.org/10.1143/JJAP.47.7311

[6] Dang, G. T., Shinohara, D., Higashiwaki, M., and Fujita, S., Bandgap engineering of α-$(Al_xGa_{1-x})_2O_3$ by a mist chemical vapor deposition two-chamber system and verification of Vegard's law, Applied Physics Letters, vol. 113, Aug. 2018, Art. no. 062102. https://doi.org/10.1063/1.5037678

[7] Guo, H., Zhao, Y., Chen, Z., Liu, J., Wang, J., and Wei, J., Applications of AlGaN/GaN high electron mobility transistor-based sensors in water quality monitoring, Semiconductor Science and Technology, vol. 35, no. 12, Oct. 2020. https://doi.org/10.1088/1361-6641/abb8fb

[8] Wang, T., Zhao, Y., Zhang, Z., Guo, Y., and Sun, H., Band gap and band offset of $Ga_2O_3$ and $(Al_xGa_{1-x})_2O_3$ alloys, arXiv preprint, Jun. 2018 in Physical Review Applied, vol. 10, 2018, Art. no. 011003. https://doi.org/10.48550/arXiv.1806.03360

[9] Newnham, R. E., de Haan, Y. M., and Meagher, E. P., Refinement of the α-$Al_2O_3$, $Ti_2O_3$, $V_2O_3$ and $Cr_2O_3$ structures, Zeitschrift für Kristallographie, vol. 117, iss. 2–3, pp. 235–237, Aug. 1962. https://doi.org/10.1524/zkri.1962.117.2-3.235

[10] Mu, S., and Van de Walle, C. G., Phase stability of $(Al_xGa_{1-x})_2O_3$ polymorphs: a first-principles study, Physical Review Materials, vol. 6, Oct. 2022, Art. no. 104601. https://doi.org/10.1103/PhysRevMaterials.6.104601

[11] Giannozzi, P., Baroni, S., Bonini, N., Calandra, M., Car, R., Cavazzoni, C., Wentzcovitch, R. M., Quantum ESPRESSO: a modular and open-source software project for quantum simulations of materials, Journal of Physics: Condensed Matter, vol. 21, no. 39, Art. no. 395502. https://doi.org/10.1088/0953-8984/21/39/395502